This article has been accepted for publication in IEEE Transactions on Biomedical Circuits and Systems. This is the author's version which has not been fully edited and content may change prior to final publication. Citation information: DOI 10.1109/TBCAS.2022.3202026

A Fully Implantable Opto-Electro Closed-Loop Neural Interface for Motor Neuron Disease Studies

Fangqi Liu, *Member, IEEE*, Yu Wu, *Member, IEEE*, Noora Almarri, *Student Member, IEEE*, Maryam Habibollahi, *Student Member, IEEE*, Henry T. Lancashire, Barney Bryson, Linda Greensmith, Dai Jiang, *Senior Member, IEEE*, and Andreas Demosthenous, *Fellow, IEEE*,

***Abstract*—This paper presents a fully implantable closed-loop device for use in freely moving rodents to investigate new treatments for motor neuron disease. The 0.18 µm CMOS integrated circuit comprises 4 stimulators, each featuring 16 channels for optical and electrical stimulation using arbitrary current waveforms at frequencies from 1.5 Hz to 50 kHz, and a bandwidth programmable front-end for neural recording. The implant uses a Qi wireless inductive link which can deliver >100 mW power at a maximum distance of 2 cm for a freely moving rodent. A backup rechargeable battery can support 10 mA continuous stimulation currents for 2.5 hours in the absence of an inductive power link. The implant is controlled by a graphic user interface with broad programmable parameters via a Bluetooth low energy bidirectional data telemetry link. The encapsulated implant is 40 mm × 20 mm × 10 mm. Measured results are presented showing the electrical performance of the electronics and the packaging method.**

Keywords*— *Implantable devices, integrated circuits, motor neuron disease, neural recording, opto-electro stimulation, optogenetics.

I. Introduction

Developing implantable microelectronic neural interface devices for interacting with the nervous system may contribute to promising solutions for treatment of neurological disorders. In motor neuron disease (MND) the illness causes progressive degeneration of motor neurons and damage to the pathway to the central nervous system. Although engrafting motor neuron stem cells into peripheral nerve environments offers the possibility to reinnervate denervated muscles [1], the pathway from engrafted neurons to the central nervous system is still missing. Performing functional electrical stimulation may help restore the communication pathway between the peripheral and central nervous system. However, due to the relatively large size and material limits of the electrodes, the generated local electrical fields can excite both the target and peripheral neurons (e.g. endogenous and engrafted neurons) causing considerable discomfort. Recent research in genetically modified cells with ion channels [channelrhodpsin2 (ChR2)] that are sensitive to light provided the novel approach of 'optogenetics' [2]. The spreading area of the modification can be defined by the virus types [3] and the specificity (excitatory or inhibitory) of neuronal populations targeted can be identified using cell-type specific promoters. Optogenetics offers the possibility of specifying the affected neurons, providing a powerful method for neuro stimulation [4].

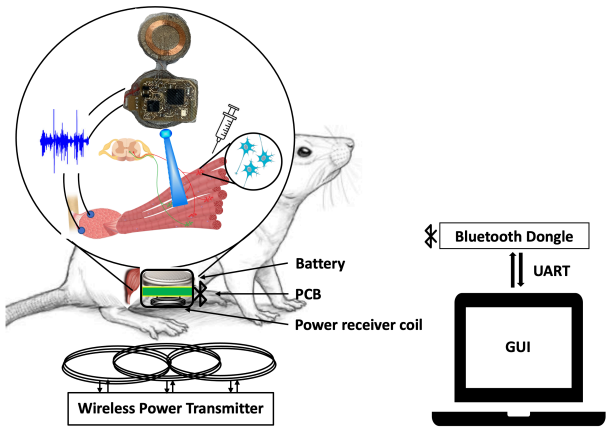

Fig. 1. Conceptual diagram of closed-loop optogenetic/electrical stimulation for treating motor neuron disease using stem cell-derived motor neurons.

A novel approach combining stem-cell neural regeneration and an optogenetics neural interface shows encouraging evidence in rodent tests. It suggests an effective treatment for MND [5], where stem-cell derived motor neurons can be activated by closed-loop optical stimulation after reinnervating the target muscle units, as shown in Fig. 1. A long survival time of both the animal and the implant is required due to the slow progress of the reinnervation of the engrafted stem-cell motor neurons. A fully implantable device: 1) helps to extend the survival time of the rodent as it reduces risks of infection and immunoreactivity [6] [7]; 2) allows maximum flexibility for designing studies with freely moving rodents; and 3) may support the reinnervation of the stem-cell motor neurons.

To study the dynamic modulation of neuron activities, a small fully implantable closed-loop implant with versatile stimulation settings and real-time recording is required. The stimulation must be precisely controlled with adjustable parameters to meet safety requirements (e.g. charge balance) [8] and capable of delivering a modulated stimulation

Manuscript received 04 April, 2022. This work was supported in part by the UK Medical Research Council, UK Research and Innovation, under Grant MR/R011648/1, and the European Union's Horizon 2020 Research and Innovation Program under Grant 824071. (*Corresponding author*: Andreas Demosthenous.)

F. Liu, Y. Wu, N. Almarri, M. Habibollahi, D. Jiang and A. Demosthenous are with the Department of Electronic and Electrical Engineering, University College London, WC1E 7JE London, U.K. (e-mail: fangqi.liu.14@ucl.ac.uk; a.demosthenous@ucl.ac.uk).

H. T. Lancashire is with the Department of Medical Physics and Biomedical Engineering, University College London, WC1E 6BT, London, U.K.

B. Bryson and L. Greensmith are with the Department of Neuromuscular Diseases, UCL Institute of Neurology, Queen Square, London WC1N 3BG, UK.

This article has been accepted for publication in IEEE Transactions on Biomedical Circuits and Systems. This is the author's version which has not been fully edited and content may change prior to final publication. Citation information: DOI 10.1109/TBCAS.2022.3202026

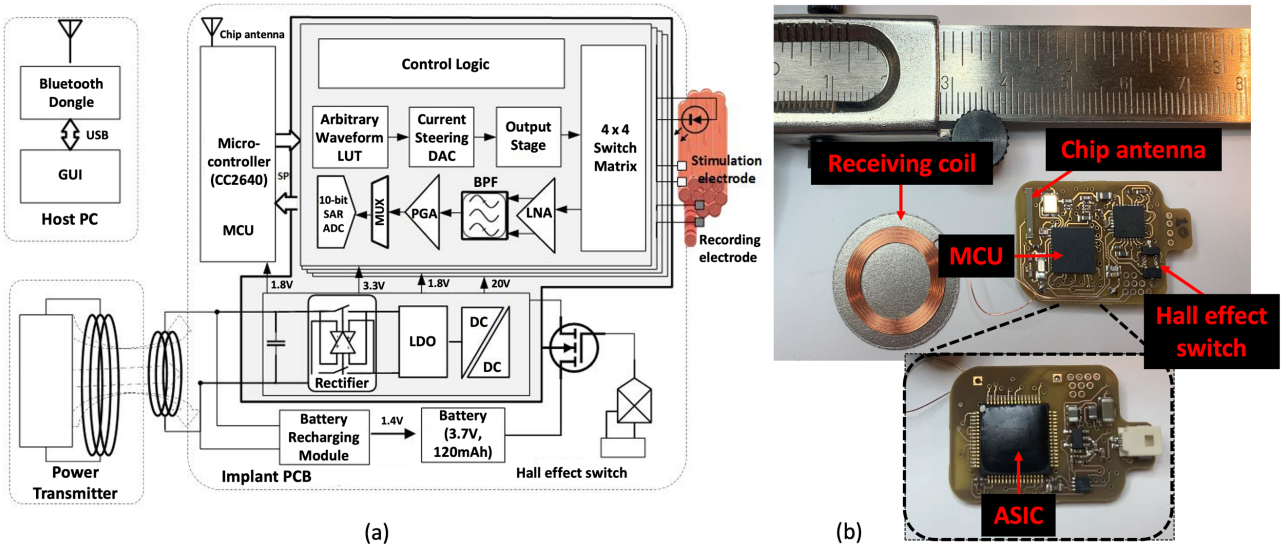

Fig. 2. (a) Architecture of the opto-electrode implant system (the ASIC is marked in grey). (b) Fabricated implant PCB with receiving coil.

waveform for optimized stimulation (e.g. improving charging efficiency and fiber selectivity) [9], [10]. Animal studies show that hybrid optogenetic and electrical stimulation significantly improves stimulation efficacy [11]. There is emerging demand for an implantable system with this hybrid stimulation. Since the activities of neurons are well represented in local field potentials [12], [13], the device must also have a recording front-end with a reliable wireless communication link. The link must have sufficient signal strength after being implanted to compensate for radio signal degradation caused by the skin and tissues. In addition, optogenetic stimulation requires intense light to evoke the neuron activities but the light scatters strongly in neural tissue. In behavioral studies, the required light intensity is up to 600 mW/mm^2 [14]. The stimulation interface must deliver intense light energy concomitant with potential power and safety constraints.

In literature, a popular approach to optogenetic stimulation is to develop devices that are surface mounted on the rodent. The implantable μLED and electrodes are percutaneously connected with an external device. Since the control and powering circuits can be implemented in an external device, the design challenges of power supply, size and temperature constraints are reduced. In [15] an optical stimulation platform was reported with electrophysiology recording. The implantable optical fibers and recording electrodes are connected with the external device via a miniature Omnetics connector. Similar approaches [16]–[19] were successfully implemented in animal tests. However, the demonstrated devices required cables or adaptors connected to the external device. Therefore, the risks of infection are increased and bring challenges for long-term in-vivo tests. Although the size and weight of the external device can be minimized to reduce its influence on animal movement, mounting an external device has disadvantages of breakage of cables, causing discomfort and stress to the rodent which might degrade the results in MND studies.

To overcome the unreliability of percutaneous connections, fully implantable optical stimulation interfaces have emerged. An RF-powered fully implantable optoelectronic device manufactured on polymer filaments was reported in [20]. It was successfully implemented in in-vivo tests in mice with promising results. However, the device was designed based on passive electronics that cannot offer flexible control of stimulation frequency and waveform shape that are important for optogenetic studies. Fully implanted optical stimulation platforms with controllable stimulation parameters facilitated by an application specific integrated circuit (ASIC) on the implant, were presented in [21], [22]. However, these devices can only provide limited control parameters to the stimulation. The systems were designed for optical stimulation only and cannot provide the intense power required for efficient optogenetic stimulation. In addition, they do not offer recording facilities, important for optogenetic studies and treatment.

This paper presents a fully implantable multi-channel stimulating and recording implant for closed-loop opto-electro stimulation in rodents (rats). Previous papers only briefly introduced the design considerations of the ASIC [23] and the overall system [24]. This paper presents an improved ASIC with an integrated analog to digital converter (ADC), having lower noise and a broad bandwidth. The design details of each part of the system and the results of carefully designed experiments are presented. The encapsulation process is introduced with implantation feasibility test results.

The rest of the paper is organized as follows. Section II presents the overall architecture of the system. Section III describes the design details and considerations of the ASIC. Section IV presents the design of the data and power telemetry link. Section V describes the encapsulation details. Section IV presents the experiments and results for evaluating the performance of the system. Comparison to the state-of-the-art is discussed in Section VI. Concluding remarks are drawn in Section VII.

II. System Architecture

The overall architecture of the system is shown in Fig. 2. The system comprises the implant PCB with the ASIC for opto-

This article has been accepted for publication in IEEE Transactions on Biomedical Circuits and Systems. This is the author's version which has not been fully edited and content may change prior to final publication. Citation information: DOI 10.1109/TBCAS.2022.3202026

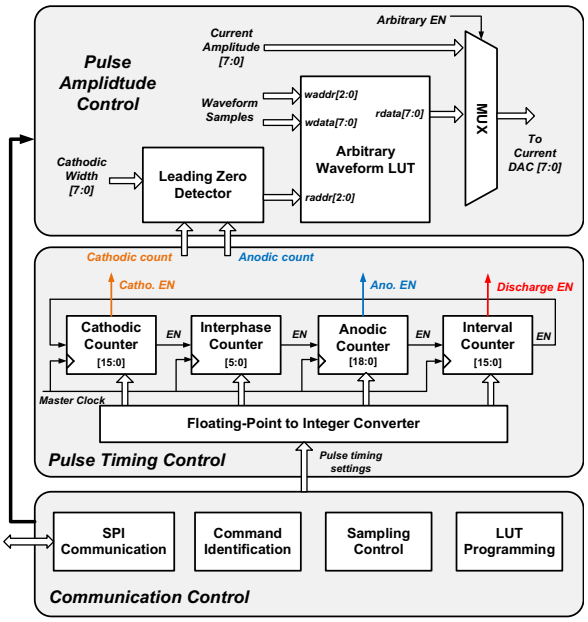

Fig. 3. Control logic in each integrated stimulator unit.

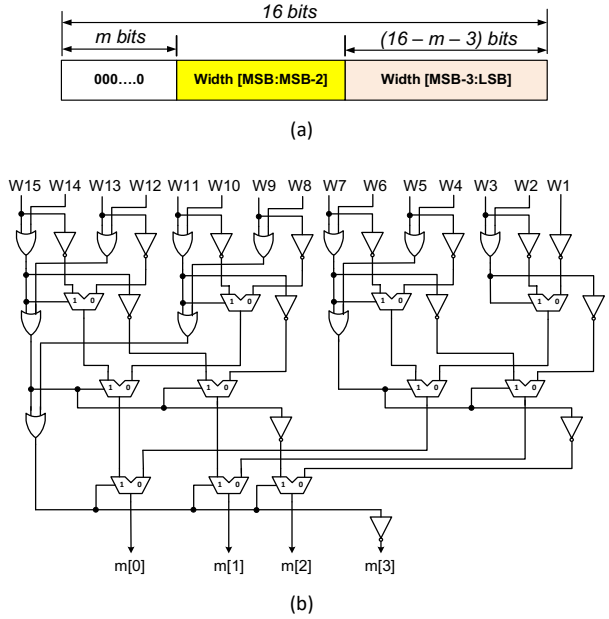

Fig. 4. Readout logic for the arbitrary waveform generator: (a) Illustration of the readout address of the look-up table; (b) Schematic of the leading zero detector.

electro stimulation and recording, a wireless power transmitter, and a host PC that remotely controls the implant. A Bluetooth Low Energy (BLE) dongle is connected to the PC via a USB cable. Dedicated software with graphic user interface (GUI) enables the user to control the stimulation settings and receive recorded EMG signals from the implant. There is a Bluetooth microcontroller (CC2640) on the implant PCB. It controls the stimulation of the implant according to the parameters from the host PC and wirelessly transmits the recorded data back. The communication between the microcontroller and the ASIC uses serial peripheral interface (SPI).

The implant is wireless powered by a Qi inductive link. The power transmitter has adaptive transmitting power adjusting for changes to the coil-to-coil distance as the test rodent moves. To ensure reliable power supplies during rodent tests, the device is also equipped with a rechargeable battery. The output of the battery is controlled by a Hall effect power switch, which can be remotely turned on/off using a magnetic stick. The switch is used to deactivate the implant during encapsulation and transportation. It also can be used to reset the BLE when a software failure occurs.

III. The ASIC

The integrated stimulator ASIC in Fig. 2 comprises four parallel stimulator units, each consisting of a 11-bit current driver and a 4 × 4 channel output stage for multi-channel optical or electrical stimulation, a 2-stage amplifier for EMG recording, and a control logic module for managing the operation. There is also a 10-bit SAR ADC multiplexed among the four stimulator units, and a global power management unit consisting of a regulating rectifier that converts the received ac voltage over the inductive link into a stable 3.3 V dc supply [25], a charge-pump dc-dc converter to step up the supply voltage to 12 V for the output stage, and a 1.8 V linear voltage regulator for supplying the low voltage modules.

A. Control Logic

The control logic in each stimulator unit operates from a 1.8 V supply at a 100 kHz master clock generated by an on-chip RC oscillator. The architecture of the logic is shown in Fig. 3.

1) Communication Control: The control logic modules in all four stimulator units receive the operation commands from the microcontroller via SPI. Each stimulator unit is assigned a hard-wired ID on-chip. The stimulator units first receive a group number via SPI. After the group assignment, operation command frames headed with group numbers are sent to all the stimulator units, and stimulator units assigned with matching group numbers respond with specified operations. This arrangement allows any number of stimulator units to perform synchronized stimulation when required. The SPI commands specify the amplitude and timing of pulsatile stimulation and the stimulating electrodes/LEDs, the amplifier gain and bandwidth for recording, and the sampling rate and multiplexing of the ADC, which is operated in the SPI slave mode.

2) Pulse Timing Control: A finite-state machine with four counters cascaded in a ring, controls the time length of a biphasic pulse and the interval between pulses, as shown in Fig. 3. Each counter counts from 0 towards the time length set by the SPI commands. The counter resets once it reaches the set value and enables the next stage counter. The counters are 16-bit for the cathodic phase and the pulse interval, corresponding to a time length between 10 µs and 655.36 ms, with a resolution of 10 µs. This is suitable for various stimulation requirements from low frequency optical stimulation with a pulse width at the level of

This article has been accepted for publication in IEEE Transactions on Biomedical Circuits and Systems. This is the author's version which has not been fully edited and content may change prior to final publication. Citation information: DOI 10.1109/TBCAS.2022.3202026

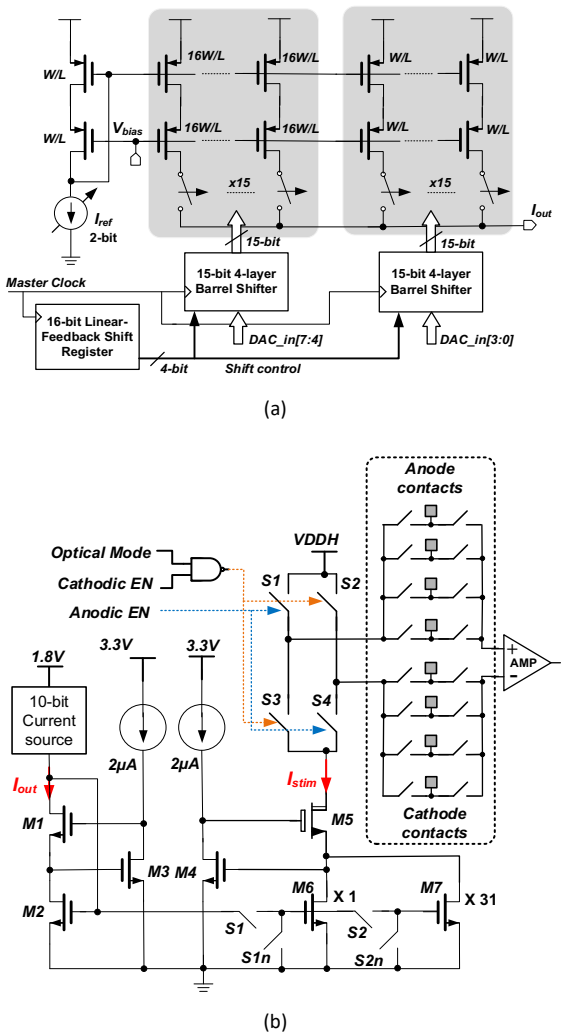

Fig. 5. Implementation of the current driver: (a) Schematic of the output stage; (b) Schematic of the 10-bit current-steering DAC.

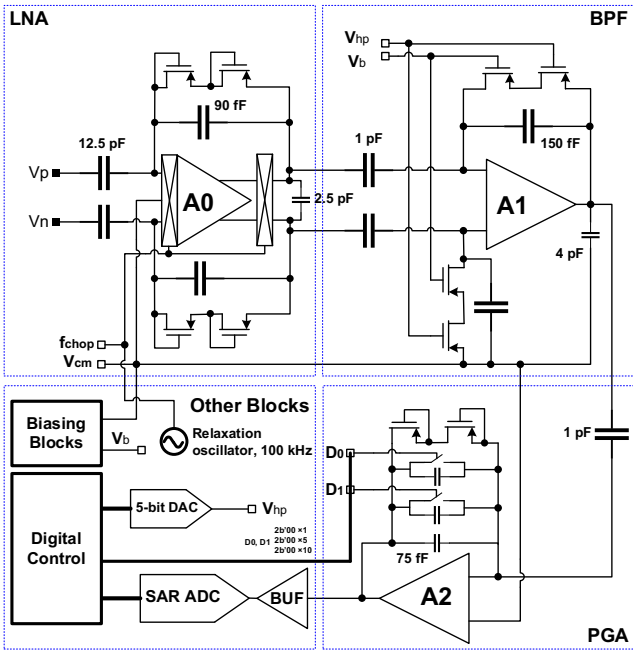

Fig. 6. Overview of the neural recording block.

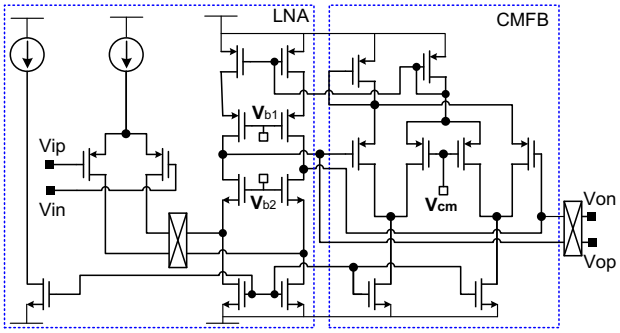

Fig. 7. First stage LNA schematic [A0 Fig. 6)].

milliseconds, to high frequency nerve blocking at > 20 kHz [26]. For symmetrical or asymmetrical biphasic pulses the anodic pulse width can be set to be equal to or eight times the cathodic pulse width. To reduce communication bandwidth demand, the pulse width and interval settings in the SPI commands are in floating-point format, *M.N*, corresponding to an integer value of $((1.N) * 2^M)_2$, where *M* is 4-bit, and *N* is 4-bit for the pulse width and 6-bit for the interval.

3) Pulse Amplitude Control: The SPI can directly set the current digital to analog converter (DAC) to generate current pulses with a constant amplitude, or program the built-in look-up table (LUT) to generate pulses with arbitrary waveforms, so that the current pulses can be shaped to improve the stimulation efficiency [27], or to measure impedance for electrode contact detection or surgical guidance [28]. The LUT stores eight 8-bit amplitude settings for a single phase of the pulse waveform. In the arbitrary waveform pulse mode, during a cathodic or anodic phase the highest three non-zero bits in the cathodic or anodic counter are used as the address for reading the LUT, as shown in Fig. 4(a). This figure shows that the specified pulse width may occupy the full 16 bits of the counter, where the highest *m* bits in the counter will remain zero during the phase. A leading zero detector circuit [29], shown in Fig. 4(b), can derive the number of the leading zeros, *m*, from the pulse width setting value after the setting is converted from the floating-point format to the 16-bit integer format, so that the highest three none-zero bits in the counter can be accurately located to be used as the LUT reading address.

B. Current Driver

The current driver comprises an 8-bit current-steering DAC with a 2-bit programmable current reference, shown in Fig. 5(a), and an output stage with a wide-swing current mirror driving an H-bridge output, shown in Fig. 5(b). The current steering DAC has two sections of equal weight groups, each consisting of 15 identical current branches. The ratio between the branches in the two groups is 16:1. The two groups are driven by the four MSBs and four LSBs of the 8-bit output from the pulse amplitude control. The 4-bit input to each group is converted to a 15-bit branch control via a 4-layer barrel shifter, whose rotation is controlled by a pseudorandom sequence generated by a 16-bit linear-feedback shift register [30]. This arrangement can randomize the nonlinearity in the current DAC output caused by mismatch between the current branches.

This article has been accepted for publication in IEEE Transactions on Biomedical Circuits and Systems. This is the author's version which has not been fully edited and content may change prior to final publication. Citation information: DOI 10.1109/TBCAS.2022.3202026

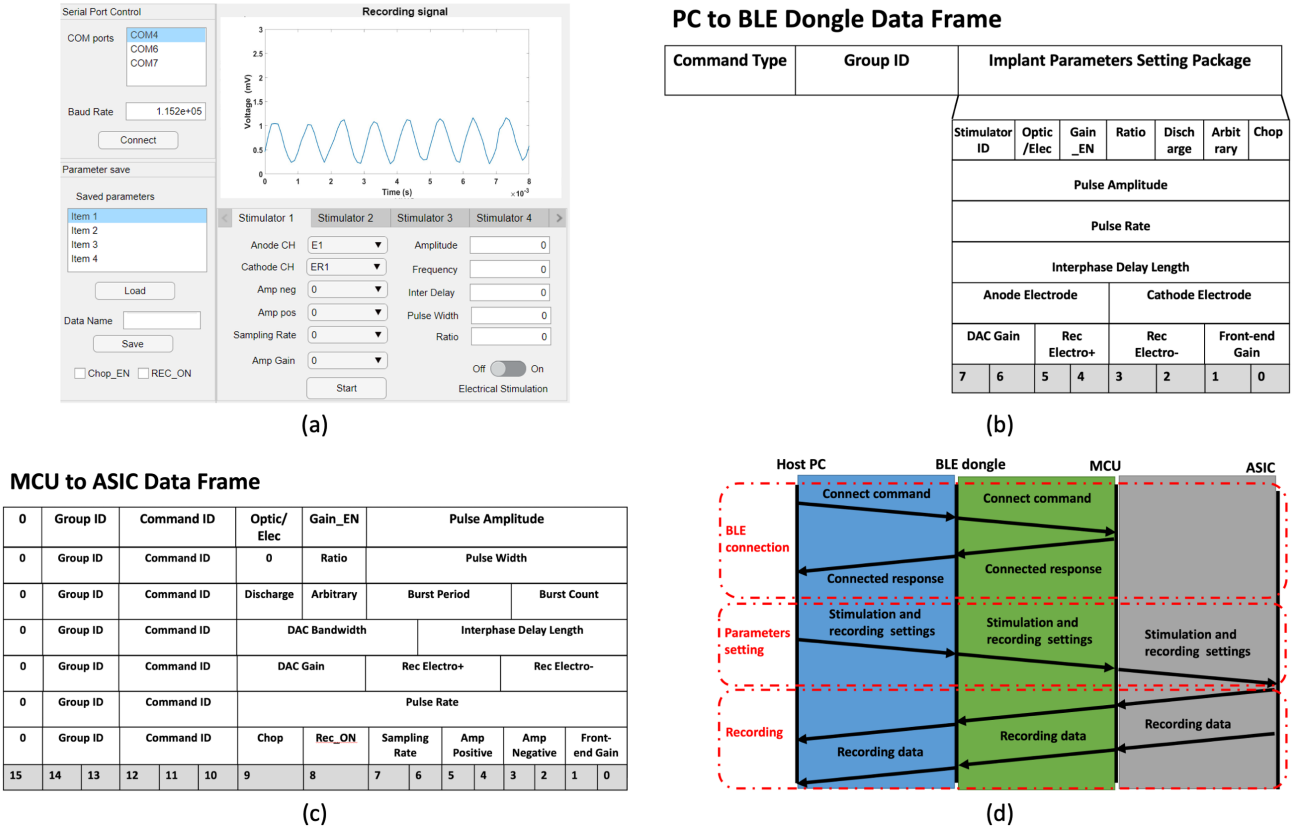

Fig. 8. (a) Developed MATLAB based GUI. (b) Data frame for communication between the host PC and BLE dongle. (c) Structure of the data frame for communication between the MCU and ASIC. (d) Overall communication structure between the host PC and the implant.

The 2-bit current reference provides a current from 500 nA to 2 µA for the current DAC. In addition, the wide-swing current mirror in the output stage can further boost the output current by 32 times, as shown in Fig. 5(b). Therefore, the total output current amplitude, I_{out}, is

$$I_{\text{out}} = 32^{A[10]} \times (16 \times A[9:6] + A[5:2]) \times (A[1:0] + 1) \times 500 \text{ nA}. \quad (1)$$

The wide dynamic range of the output current allows up to 16 mA for driving the LEDs to achieve the light intensity for exciting the engrafted motor neurons, and small current amplitudes at the µA level for electrical stimulation or below the neural excitation threshold for impedance measurement. The output current is shaped into a biphasic or monophasic pulse, depending on whether electrical or optical stimulation is chosen, by the H-bridge supplied from the high voltage VDDH provided by the charge-pump dc-dc converter. The stimulation mode control, the current reference setting and the current boost setting, are specified in the SPI commands.

C. *Neural Front-End*

The analog recording front-end consists of three stages, as shown in Fig. 6. The first stage is a low-noise amplifier (LNA) A0, with chopping to reduce flicker noise. It has a gain of 100 set by the ratio between the feedback and input capacitors. The second stage, A1, provides differential-to-single conversion and band-pass filtering (BPF) with an upper cut-off frequency of 4 kHz. The lower cut-off frequency can be programmed by varying the gate voltage (V_{hp}) of the feedback pseudo-resistor [31], where V_{hp} is provided by a 5-bit DAC controlled by the digital block. The BPF can offer a lower band from 1 Hz for EMG recording to 100 Hz for AP recording. The third stage is a programmable gain amplifier (PGA) A2. By setting the switches across the feedback capacitors using D0 and D1, the PGA gain varies from 1 to 10, changing the total gain of the recording front-end from 500 to 5000.

The detailed schematic of the LNA is shown in Fig. 7. It uses a fully differential folded-cascode OTA. Flicker noise is minimized by enlarging the size of its input transistor pair. Although chopping before the input of the OTA will further reduce flicker noise, it can lead to an unacceptably large input capacitance [32]. The chopping is placed at the OTA's folded low-impedance node; this design aims to reduce the flicker noise of the OTA's active load while allowing the chopping frequency to be higher than 100 kHz, which the following BPF stage can easily filter out.

A biasing block (shown in Fig. 6 left side) provides all the required fixed bias voltages, and a relaxation oscillator is designed to provide the chopping signal at 100 kHz internally. The output of the neural recording front-end is digitized using a 10-bit SAR ADC.

D. *Power Management*

An active full-wave rectifier featuring feed-back regulation was implemented to convert the ac voltage from the inductive

link into a 3.3 V dc supply. The gate controls of the PMOS power switches in the active rectifier are multiplexed between two sources. The first is from two high-speed common-gate comparators that compare the input ac voltage from the receiver coil to the rectifier output dc voltage. The second is the input ac voltage directly. The multiplexing is controlled by a feedback loop comprising an error amplifier and a pulse width modulation (PWM) controller [42]. The output dc voltage from the rectifier is compared to a reference voltage, and the difference is amplified by the error amplifier. The error amplifier output is then compared with a ramp signal to generate a continuous train of pulses that functions as the multiplexer control, where the pulse width varies with the rectifier output voltage. This ensures the rectifier output remains stable at 3.3 V, despite possible voltage variations over the inductive link.

The 3.3 V output is up-converted to 12 V by a 3-stage cross-coupled charge-pump for the stimulator output stage, and down-converted to 1.8 V by a linear regulator. The details of the power management unit are provided in [25]. With a 1 kΩ load under a 6.56 MHz input, the voltage conversion efficiency (VCE) and power conversion efficiency (PCE) of the regulating-rectifier are 87.5% and 84.2%, respectively. Under a 127.6 kHz input the efficiency of the VCE and PCE with the same load are 85.4% and 86.3%, respectively.

IV. Wireless Data And Power Telemetry

To collect sufficient information for medical diagnostics and neuroscientific studies, optogenetic experiments often require precise control of stimulation waveform patterns, parallel processing of many stimulators at the same time, and electrical recording of any neuron response [8]. The proposed data telemetry link is designed to be capable of precisely controlling multichannel parallel stimulation and receiving the recorded EMG signal in real-time. The power telemetry link provides a reliable power supply for system operation and intensive stimulation while also allowing free rodent movement to minimize the need for prior habituation and handling of rodents in in-vivo tests.

A. Graphic User Interface (GUI)

A GUI for controlling stimulation and recording settings was designed using MATLAB (R2019b) App Designer as shown in Fig. 8. To achieve parallel control of multi-channel stimulation with a broad parameter range, the specific electrodes can be selected under different stimulation channels setting tags. For stimulation, either optical or electronic stimulation mode can be selected. The stimulation amplitude, pulse ratio, pulse width, length of inter phase delay, and stimulation frequency can be set by typing in the appropriate parameters. The GUI is able to set arbitrary simulation waveforms by setting the pulse shape parameters. For recording, the bandwidth, sample rate, chopping and gain of the DAC can be adjusted. By pressing the start button all the parameters will be sent to the implant and the GUI will display the recorded EMG signal in real-time. All the set parameters and recorded data can be saved as a MALTAB data file which can be loaded directly in later experiments.

B. Data Telemetry

Bidirectional data telemetry between the host PC and the implant was designed to remotely control the implant and receive the recorded EMG signals. For the downlink data telemetry, the implant setting parameters are sent to the wireless microcontroller unit (MCU) (CC2640 Texas Instrument, US) dongle via the UART at a baud rate of 115200 bps. The data frames are shown in Fig. 8(b). The data starts with a 2-bit task type characterization byte to notify the BLE dongle to either connect or disconnect the BLE for transmitting controlling parameters. Then, the group ID is used to combine different stimulators and electrodes as the same group for parallel stimulation. The rest of data are implant controlling parameters, which are packaged into 6 × 8 bit frames. The BLE dongle converts the UART data to RF signals following the BLE 5.1 protocol. The RF signal is received by the BLE based MCU on the implant and converted into SPI based data frames to be transmitted to the ASIC at a clock frequency of 8 MHz. The data frames for SPI communication are shown in Fig 7(c). The command ID is used to notify the register address of each group of settings. In each of the setting processes, 8 ×16 bits data are sent to the ASIC.

For the uplink data telemetry, the ADC in the ASIC samples the EMG signal on the electrodes and transmits to the MCU via the SPI at the clock frequency of 10 MHz. The MCU counts the buffer size on the fly and an I/O input interrupt will be generated when the buffer is half full. The interrupt triggers the BLE notifications to transmit the EMG signal back to the BLE dongle at the PC site. Then, the BLE dongle sends the recorded data to the host PC via the UART at a baud rate of 115200 bps.

A standard data telemetry process is shown in Fig.8 (d). The host PC sends a BLE connection command to the BLE dongle. The BLE dongle searches the BLE of the implant and asks for connection. After a successful connection, a confirmed command will be sent back the host PC. Then, the user can set the stimulation and recording parameters on the GUI. On pushing the start button on the GUI, the parameters will be transmitted out. The stimulation will start immediately after the ASIC on the implant receives the parameters.

C. Power Telemetry

The Qi standard based commercial inductive transmitter (STEVAL-ISB047V1) was adopted as the wireless power transmitter. The transmitter can deliver up to 5 W power with a carrier frequency of 126.7 kHz. The transmitter contains three transmitting coils which can recharge the battery in the implant in a rodent with free movement. A commercial inductive coil (WR222230-26M8-G) was used as the power receiving coil as it is a small size suitable to be mounted on the implant PCB. Another consideration for using a commercial fabricated coil is that its physical structure is more reliable than customized coils which helps to reduce the tuning variation due to coil shape changes during silicon curing. The inductive link was designed to work at a coil-to coil distance of between 1 cm and 2 cm to account for the implant depth variation. To improve the system stability, a 3.6 V rechargeable lithium-ion coin battery (LIR2450) with a diameter of 24 mm is used as the power backup when there is wireless powering failure. The battery can be remotely charged using the recharging module (LTC3331) at the floating voltage of 4.1 V. The fully charged battery along

This article has been accepted for publication in IEEE Transactions on Biomedical Circuits and Systems. This is the author's version which has not been fully edited and content may change prior to final publication. Citation information: DOI 10.1109/TBCAS.2022.3202026

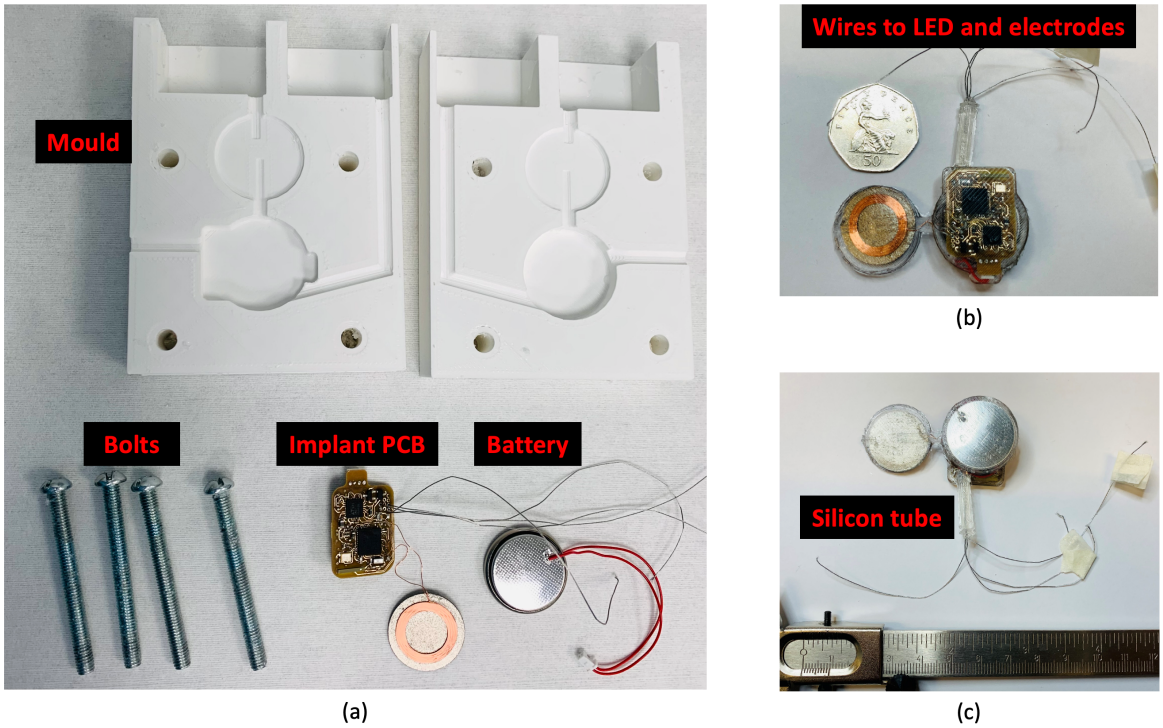

Fig. 9. Details of the implant packaging. (a) Cleaned mould, implant PCB, battery and the bolts for encapsulation. (b) Front side of the encapsulated implant with the wires to the LED and electrodes. (c) Back side of the encapsulated implant and the silicon tube.

can deliver 10 mA, 50 % duty circle stimulation current at 50 Hz for 2.5 hours.

V. Implant Packaging and Encapsulation

The dimensions of the 4-layer implant PCB are 28 mm × 19 mm (shown in Fig. 2(b)). The PCB was fabricated without resist and silkscreen and with exposed copper traces to improve encapsulation adhesion. The PCB was connected to the electrodes and LED via multistrand fluoropolymer insulated stainless steel Cooner wire (AS632, Cooner Wire Company, Chatsworth, CA, United States). The connection wires were threaded through 1 mm bore silicone rubber tubes to form implantable cables. In this study, only two pairs of electrode connection cables were formed, one for electronic-optic stimulation, the other is for recording.

The implant system was carefully cleaned before encapsulation as cleanliness is essential for survival of chronic implants [32], [33]. The implant PCB and inductive link receiver coil were cleaned by sequential washes in de-ionized water, acetone, and de-ionized water using an ultrasonic wash machine. The battery was washed twice in de-ionized water. The battery voltage was measured before and after washing. The voltage dropped by about 0.01 V. After the rinse process, the conductivity of the rinse solution was monitored to confirm adequate cleanliness.

In the present work the implants were encapsulated using medical grade silicone rubber. A low viscosity, optically clear, two-part silicone adhesive (MED-6015, AvantorNusil, Radnor, PA, United States) was used to reduce the risk of voids and bubbles. Part A and Part B were mixed in a ratio of 1:10 using a speed mixer for 3 mins at 2500 rpm (Dual Asymmetric Centrifugal Laboratory Mixer System, DAC 150 FVZ-K, Synergy Devices Ltd). A mould was designed using Autodesk CAD (2022) and was 3D printed using polylactic acid as shown in Fig. 9 (a). The two parts of the mould were matched so that they can be clamped together using four bolts. Before encapsulation, the mould is cleaned in de-ionized water with the assistance of ultrasound. The implant was held in the centre of the mould using pre-formed silicone spacers. The implant was encapsulated under vacuum (50 mBar) in a centrifuge (up to 200 g) to remove air bubbles. Due to the temperature limitations of the battery, the silicone rubber was cured at room temperature (21 °C) for at least 48 hours. The encapsulated implant is shown in Fig. 9(b) and (c).

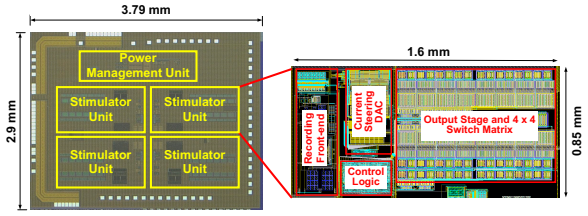

Fig. 10. Stimulator chip micrograph and details of each stimulator unit.

VI. Results

The stimulator ASIC was implemented in XFAB 0.18 µm HV CMOS technology with a size of 3.79 mm × 2.9 mm. Fig. 10 shows a micrograph of the ASIC alongside the layout details of a single stimulator unit. The measured current consumption on the 1.8 V supply is 636 µA when one stimulator unit is in a

This article has been accepted for publication in IEEE Transactions on Biomedical Circuits and Systems. This is the author's version which has not been fully edited and content may change prior to final publication. Citation information: DOI 10.1109/TBCAS.2022.3202026

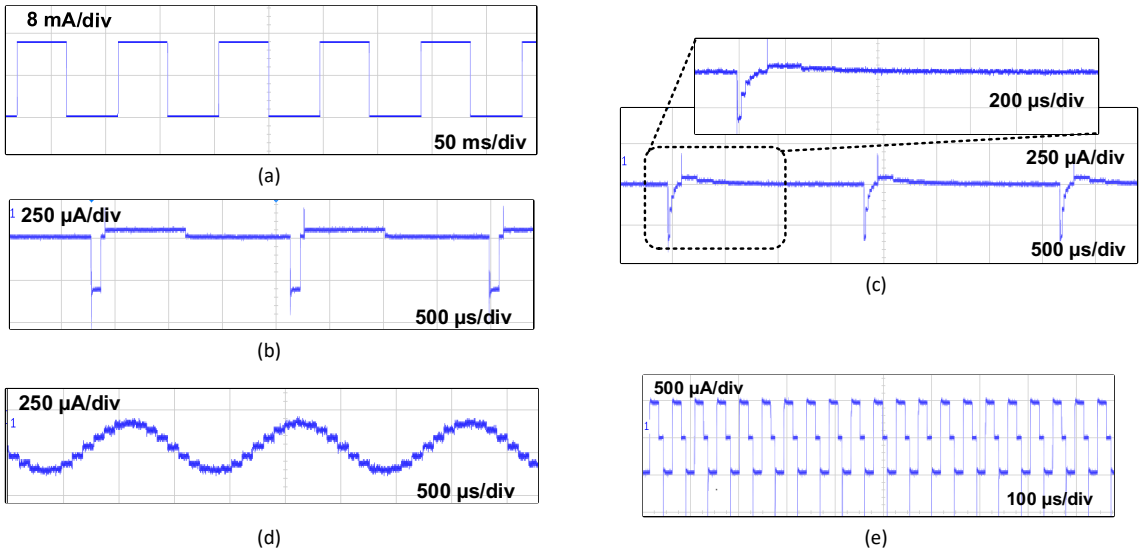

Fig. 11. Examples of measured current pulses generated by the stimulator.

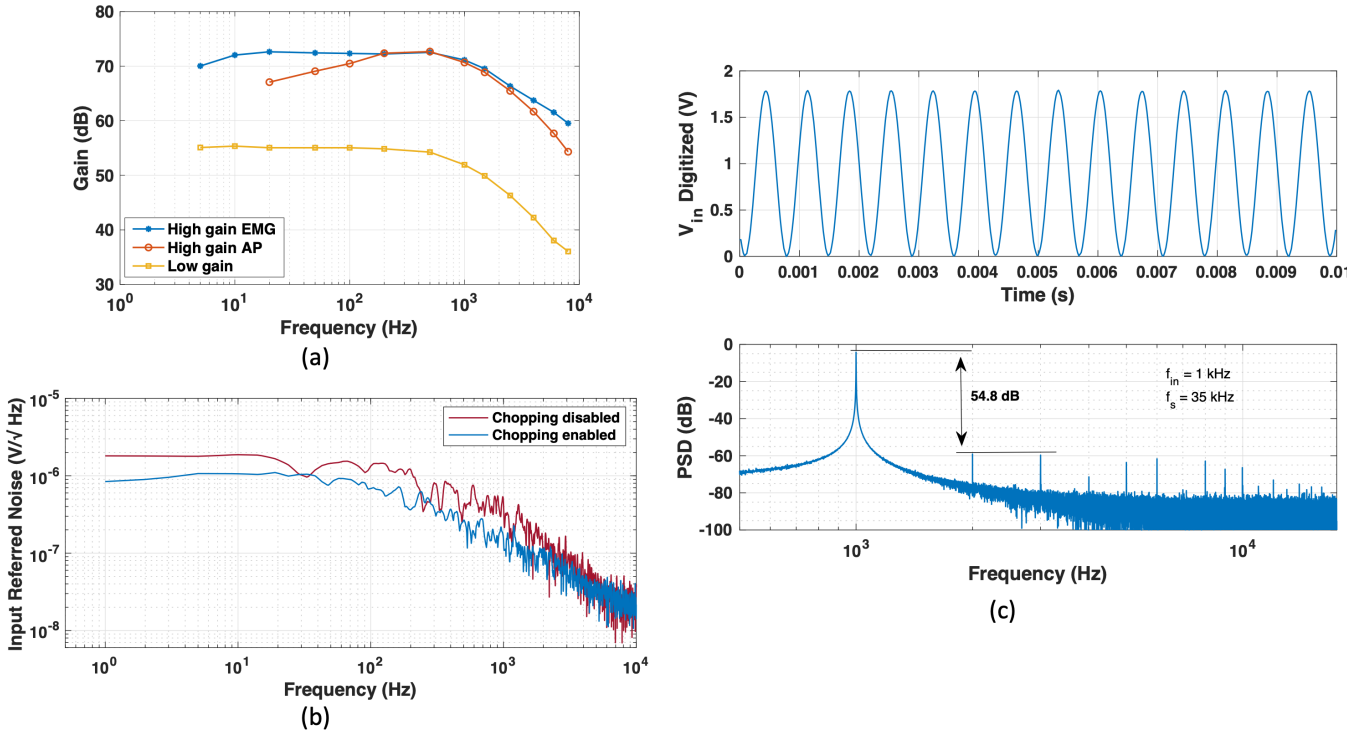

Fig. 12. Measured perfomrance of the recording front-end: (a) Measured frequency response of the 2-stage amplifier with different gain and bandwidth configurations. (b) Measured input-referred noise with the highest gain setting and frequency up to 10 kHz. (c) Digitized input test signal (top) and its FFT plot.

full operating mode, and generates 16 mA, 48 ms monophasic pulses at 10 Hz, recording with a ×5000 gain and digitized at 35 kS/s. With stimulation disabled, the measured current consumption on the 1.8 V is 120.5 µA for the four 2-stage amplifiers, ADC, biasing units and I/Os.

A. Stimulation

Fig. 11 shows examples of output current waveforms for different purposes measured with an oscilloscope (Keysight, MSOX3014T). Fig. 11(a) shows 10 Hz, 48% duty cycle monophasic current pulses at a 15-mA peak amplitude for optical stimulation. Fig. 11(b) shows charge-balanced, asymmetrical biphasic pulses at a constant current amplitude of 256 µA in the cathodic phase and 32 µA in the anodic phase. Fig. 11(c) shows a charge-balanced, asymmetrical biphasic pulse programmed for an exponential shape, with the details of pulse amplitude change in a single phase shown in the zoomed-in window. Both the pulse shapes in Fig. 11(b) and (c) are for electrical stimulation. Fig. 11(d) shows the output current programmed into a sinusoidal waveform at 666 Hz for impedance measurement, and Fig. 11(e) shows 500 µA biphasic pulses at 25 kHz for nerve blocking.

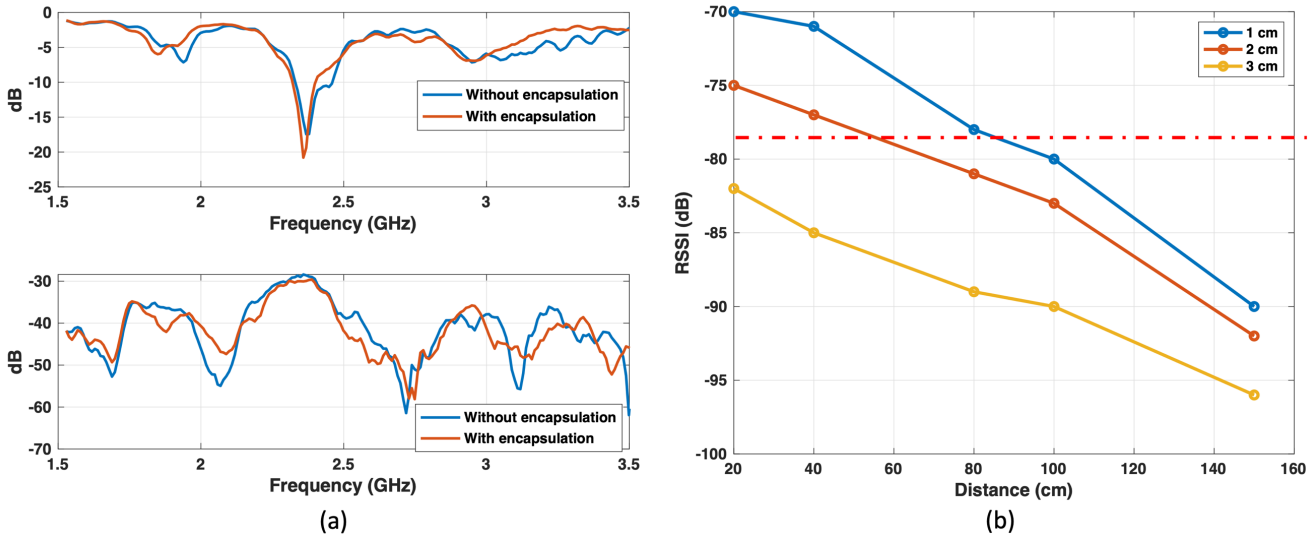

Fig. 13. (a) Measured return loss (S11) of the antenna as a function of frequency with (in orange) and without (in blue) encapsulation. (b) Measured S12 of two identical antennas as a function of frequency with (in orange) and without (in blue) encapsulation. (c) RSSI of the implant Tx signal at implantation depth of 1 cm (marked in blue), 2 cm (marked in orange) and 3 cm (marked in yellow) as a function of communication distance.

TABLE I. REQUIRED TRANSMITTING POWER OF INDUCTIVE LINK

Coil Distance (cm)	Transmitting Power (W)	
	Minimum	Maximum
1	0.4	1.8
2	1	7.3
3	5.4	N/A

B. *Recording*

The frequency response of the recording front-end was measured with an oscilloscope (Keysight, MSOX3014T) at the highest gain setting (D1-D0 2b'00), and the lowest gain setting (D1-D0 2b'10) with a bandwidth of 5 Hz to 8 kHz as shown in Fig.12(a). By controlling the 5-bit DAC, the high-pass can be tuned to around 100 Hz for action potential recording at the highest gain setting which was measured at 72.7 dB at passband. The lowest gain is 55 dB at passband. The common-mode rejection ratio (CMRR) was also measured from 5 Hz to 8 kHz. On average, the front-end has a CMRR of 74 dB.

The noise was measured by shorting the two inputs to ground with the high gain setting. and the results are shown in Fig.12(b). Flicker noise is reduced when the chopping is turned on. The measured input-referred integrated noise is at band-pass (BP: 100 Hz – 1.5 kHz) and wide-band (WB: 1 Hz – 4 kHz). Noise at BP is 10.2 μV_{rms} with chopping and 20.5 μV_{rms} without chopping, and at WB is 14.2 μV_{rms} with chopping and 25.7 μV_{rms} without chopping. The estimated power consumption of the analog front end is 12.2 µW.

C. *ADC Measurements*

The 10-bits SAR ADC was tested at a sampling rate of 35 kS/s, and an input signal of 1.8 V_{pp} at 1 kHz; the digitized signal is shown in Fig.12(c) (top) with its fast Fourier transform (FFT) (below). The maximum harmonics are 54.8 dB below the fundamental. Due to the integration, it was not possible to directly measure the ADC power, but the estimated power consumption is 16.2 µW.

D. *Inductive Link*

The requried transmitting power at different coil distances has been measured. The minimum transmitting power for supplying the operating power of the implant has been measured as a function of coil distance (as shown in Table I). The minimum transmitting power increased from 0.4 W to 5.4 W as the coil distance increased from 1 cm to 3 cm. In addition, the maximum transmitting power, which is decided by the maximum tolerable voltage of the receiving rectfier circuits, has also been measured (as shown in Table I).

To study the effect of the the inductive link signal absorbed by tissue, 128 grams fresh pork 13 mm thickwas placed over the transmitter coil for 1 hour. The internal temperature of the pork 5 mm from the centre of the transmission coil was measured using a temperature probe before and after the experiment. For comparison, a second 126 gm 14 mm thick piece of pork was cut from the same piece as the test sample. The two pieces were allowed to stabilise to room temperature for 1 hour before the test. The transmitting power was set to 1.8 W, the maximum transmitting power at a coil distance of 1 cm (which is the most common case in the targeted application). Before the test the measured temperature of the test sample was 21.6 ± 0.2 °C (mean and standard deviation of 5 repeat measurements), and the temperature of the control sample was 21.4 ± 0.2 °C, respectively. After 1 hour, the temperature of the test sample was 22.1 ± 0.3 °C, and of the control sample 22.0 ± 0.3°C. The temperature of both samples slightly increased compared with the starting temperature, attributed to ambient temperature change. However, there was no significant temperature difference between the test and control samples after one hour of power transmission.

E. *Bluetooth*

Two experiments were performed to estimate the quality of

This article has been accepted for publication in IEEE Transactions on Biomedical Circuits and Systems. This is the author's version which has not been fully edited and content may change prior to final publication. Citation information: DOI 10.1109/TBCAS.2022.3202026

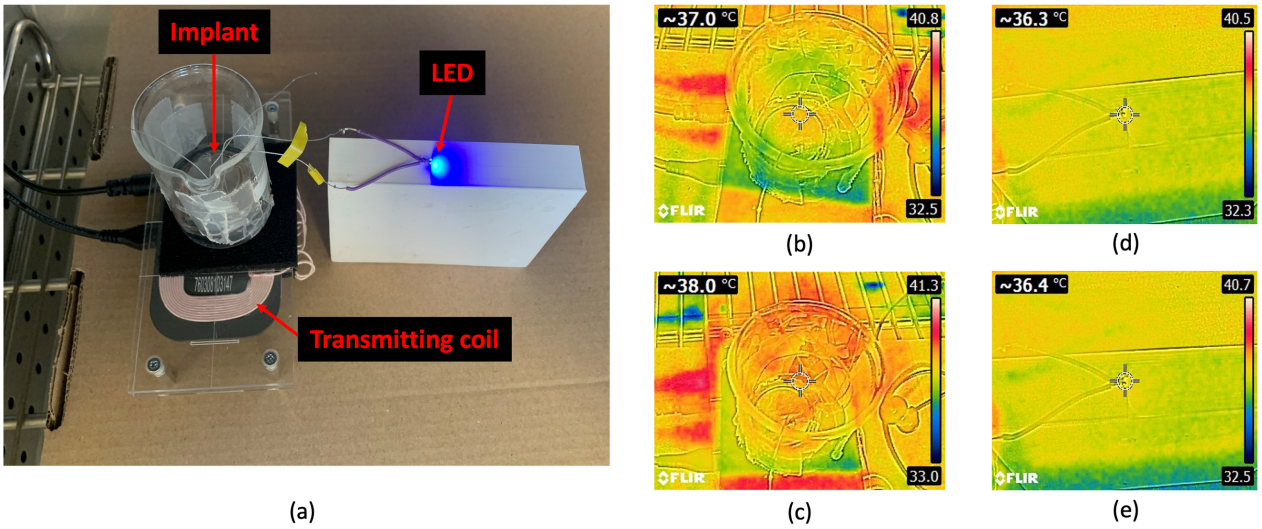

Fig. 14. (a) Implantation feasibility test set up in a climate chamber. The implant is placed in the beaker filled with deionized water. The top side surface of the implant and the LED are exposed to the air when measuring the surface temperature. (b) Measured surface temperature of the implant before stimulation. (c) Measured surface temperature of the implant after 1 hour stimulation. (d) Measured surface temperature of the LED before stimulation. (e) Measured surface temperature of the LED after 1 hour stimulation.

the data telemetry link after implantation. A one-side chip antenna (ACAG0801-2450-T) was implemented on the implant PCB (as shown in Fig. 2(b)) for Bluetooth communication. To investigate the influence of the encapsulation process on antenna properties, the antenna response before and after encapsulation was measured. The encapsulation process follows the steps provided in Section IV. The response of the antenna was measured using a vector network analyzer (ZNL6, Rohde & Schwarz). In Fig. 13(a), the upper panel shows the return loss (S11) with (marked in orange) and without (marked in blue) the encapsulation as a function of frequency. After encapsulation, the maximum return loss frequency was slightly shifted from 2.45 GHz to 2.4 GHz. The shift might be caused by a small matching impedance change at the antenna after silicone rubber encapsulated the chip antenna and the PCB track. The lower panel shows the S12 as a function of frequency using two identical antennas. The maximum response at 2.4 GHz was slightly reduced after encapsulation.

The previous approach in [24] investigated the attenuation effects of skin and tissue on Bluetooth by only covering the top of the implant. In this study, the received signal strength indicator (RSSI) of the implant when placed in a hole drilled in a pork elbow was measured. The depth of the implant in the hole was changed to study the effect of skin and tissue at different depths. Since the implant must transmit back the EMG signals which is relatively data intensive, the RSSI of the implant Tx as a function of communication distance was measured using a smart phone (iPhone XS). The RSSIs at the implant depth of 1 cm (marked in blue), 2 cm (marked in orange), and 3 cm (marked in yellow) are shown in figure 14b. The red dash line marks the package loss rate of 10%. According to the figure, the maximum work distance for Bluetooth to maintain reliable communication is 55 cm at the implant depth of 2 cm and 80 cm at the implantation depth of 1 cm. At an implantation depth of 3 cm the proposed BLE link cannot communicate adequately. Since the transmission power of the BLE antenna is 0 dBm, the absorption rate in human body

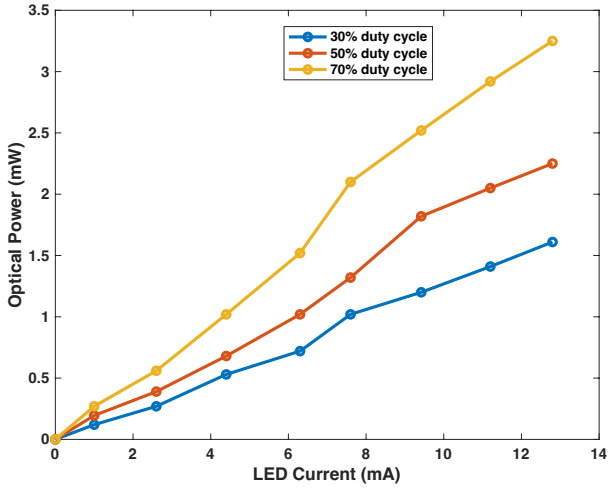

Fig. 15. Measured optical power as a function of the stimulation current on LED with duty cycle of 30%, 50% and 70%. The LED was driven by a monophasic pulse with 50% duty cycle at a frequency of 50 Hz.

is much lower than the limits (2-4 W/kg) specified in international commission on non-ionizing radiation protection (ICNIRP) [34].

F. Feasibility for Implantation

The reliability of the developed device for implantation was evaluated in a fluid environment. The implant was placed in a round bottom flask filled with de-ionized water for 7 days. The silicone rubber has low permeability to metal salts and high permeability to water vapor [35]. In the event of device failure, deionized water will accelerate the failure rate. Using deionized water is a harsher test condition for evaluating the safety of the device for implantation [36]. During the test, the implant was wirelessly powered by the transmitter. The wireless control and data telemetry of the implant was frequently checked using the GUI on the host PC.

TABLE II. COMPARISON OF MULTIFUNCTIONAL NEURAL INTERFACES

	[38]	[39]	[40]	[41]	[18]	**This work**
Technology	Commercial components	0.18 µm	Commercial components	0.18 µm	0.35 µm	0.18 µm
Stimulation channels	2	4	1	1	8	4×4×4
Stimulation current	0-1.5 mA	20 µA-5 mA	<3 mA	0-510 µA	25-775 µA	0-16 mA
Stimulation mode	Electrical	Electrical/optical	Optical	Optical & electrical	Optical	Optical & electrical
Stimulation pattern	Charge balance	Charge balance	N/A	Charge balance	Charge balance	Charge balance & arbitrary
Recording channels	2	N/A	N/A	2	16	4×4×4
Channel gain/ Bandwidth	40-120 dB/ N/A	N/A	N/A	27 dB/ up to 187 Hz	55-70 dB/ 100 Hz-10 kHz	50-73 dB/ 100 Hz-1.5 kHz, 1 Hz-4 kHz
Power supply	Inductive link/ rechargeable battery	Ultrasound	Inductive link	Battery	Inductive link	Inductive link/ rechargeable battery
Data telemetry rate	400 kbps	11 kbps	N/A	1 Mbps	6.78 Mbps	2 Mbps
Fully implantable/ Dimensions (in mm)	Yes/ 33×28×12	Yes/ 2×3×6.5	Yes/ ~10×10	No	No	Yes/ 40×20×10

The surface temperatures of both driver and a blue LED (150224BS73100 with a dominant wavelength of 456 nm), chosen for optical stimulation, were also evaluated when driving the LED at a current of 8 mA 50% duty cycle for 1 hour. To simulate body temperature, the test was done in a climate chamber (Binder KMF 155, Germany) at a constant temperature of 37 °C, as shown in Fig. 14(a). The implant was placed in a flask filled with de-ionized water, as the thermal conductivity of water (0.6 W/m/°C) is close to blood (0.52 W/m/°C) [37]. The upper surface of the implant, and the LED, were exposed in open air to provide direct access for an infrared thermal camera. Before the measurement, the setup was placed in chamber for 1 hour to allow its temperature settle to the chamber temperature. The surface temperature of the implant was measured using a FLIR E4 thermal imaging camera (FLIR systems, Wilsonville, OR, United States) with the camera perpendicularly focused on the exposed area on the implant. The surface temperatures of both the implant and the LED were measured before and after 1 hour of stimulation. As shown in Fig. 14(b) and Fig. 14(c), the surface temperature of the implant increased from 37.0 °C to 38.0 °C after 1-hour operation, and the LED temperature increased from 36.3 °C to 36.4 °C. This temperature rise is within the 2 °C safety range defined in EN 45502-1 [42] for active implantable devices.

G. Optical Power Output of LED

The optical power of the blue LED driven by a 50 cycle 50% duty cycle was measured using a photo detector (S121C, Thorlabs) connected with an optical power meter (PM100D, Thorlabs) as a function of the stimulation current. As shown in Fig. 15, the measured optical power increases with increasing stimulation current. The 70 % duty cycle shows the highest optical power of 3.24 mW at the stimulation current of 12.5 mA.

VII. COMPARISON

Table II compares the performance of the developed neural interface system with other state-of-the art work [38-41], [18]. One of the main advantages of the proposed system is that it is fully implantable. Since the motor function for chronic studies (> 2 months) is the target, the stability of the device during free movement, its reliability and usability for extended testing of the animals are essential. Although the optogenetic interfaces in [18], [41] show powerful recording functions, the recording electrodes need to be percutaneously connected to an external system to provide the power supply and data telemetry. The design challenges of size constraints to the power supply and data telemetry modules were not fully addressed. In this work, the energy harvesting module was integrated in the ASIC and the data telemetry is applied using the smaller size BLE based MCU that can be implemented into the implantable PCB.

A key feature of the proposed system is a more powerful stimulation control functionality for simultaneous closed-loop control. The implant in [39] is fairly compact but uses passive components at the expense of reduced stimulation functionality. In addition, it focused only on optical stimulation. As discussed in the introduction, an optical-electronic hybrid stimulation would contribute to improved stimulation and a powerful setting regime of stimulation waveforms is necessary in the study of the modulation of neuron signals. For example, the shape of the stimulation waveform can be set even to be arbitrary. Unlike the devices reported in literature, the proposed implant can provide simultaneous stimulation on multiple channels with versatile modality, while simultaneously recording the muscle response and communicating with a remote base station for real-time signal processing and closed-loop control.

The size of the implant is dominated by the battery. This design trade-off has sacrificed further miniaturizing in favor of providing a stable power supply to the freely moving animals under study. It also eliminates the need for a power transmitter device mounted on the animal.

VIII. Conclusion

This paper has presented a fully implantable closed-loop opto-electro hybrid stimulation system for motor neuron disease studies with freely moving rodents (rats). The system has potential to be applied for complex neuron modulation studies. The 0.18 μm CMOS ASIC consists of 4 stimulators, each featuring 16 recording or stimulation channels. The implant can delivery opto-electro stimulation using arbitrary current waveforms at frequencies from 1.5 Hz to 50 kHz, and a bandwidth programmable front-end. The implant has a small size of 40 mm × 19 mm × 10 mm. Its surface temperature increased by less than 1 °C after 1-hour continuous operation, satisfying implantable device safety range defined in EN 45502-1 [42]. The reliability of the communication link after implantation has also been tested. The rechargeable battery can support stimulation at the maximum current for 2.5 hours continuous stimulation in the absence of the inductive link.

This implantable platform will be evaluated in *in vivo* animal experiments in the near future to develop a combined therapy for treating motor neuron disease with stem-cell technology and optogenetics. Future hardware improvement of this design includes: 1) to further minimize the size of the implant by integrating the wireless data transceiver into the ASIC; 2) to develop a low-cost wireless powering platform with dynamic tracking to improve the power transfer efficiency, so that the battery could be reduced in size or eliminated; 3) to employ a low-cost packaging method, such as an injection-moulded liquid crystal polymer package [44], for extending the implantation lifetime of the device.

References

[1] D. C. Yohn, G. B. Miles, V. F. Rafuse, and R. M. Brownstone, "Transplanted mouse embryonic stem-cell-derived motoneurons form functional motor units and reduce muscle atrophy," *J. Neurosci.*, vol. 28, no. 47, pp. 12409–12418, 2008,

[2] T. A. Marie, F. Eva, R. Linda, S. O. Juan, R. Patrick, and S. Thomas, "Let there be light - Optoprobes for neural implants," *Proc. IEEE*, vol. 105, pp. 101–138, 2017.

[3] S. Y. Kim *et al.*, "Diverging neural pathways assemble a behavioural state from separable features in anxiety," *Nature*, vol. 496, no. 7444, pp. 219–223, 2013.

[4] O. Yizhar, L. E. Fenno, T. J. Davidson, M. Mogri, and K. Deisseroth, "Optogenetics in Neural Systems," *Neuron*, vol. 71, no. 1, pp. 9–34, 2011,

[5] J. B. Bryson *et al.*, "Optical control of muscle function by transplantation of stem cell-derived motor neurons in mice," *Science*, vol. 344, no. 6179, pp. 94–97, 2014.

[6] J. G. McCall *et al.*, "Fabrication and application of flexible, multimodal light-emitting devices for wireless optogenetics," *Nat. Protoc.*, vol. 8, no. 12, pp. 2413–2428, 2013.

[7] T. Kim *et al*. "Injectable, cellular-scale optoelectronics with applications for wireless optogenetics," *Science*, no. 6129, pp. 211–216, 2013.

[8] C. Günter, J. Delbeke, and M. Ortiz-Catalan, "Safety of long-term electrical peripheral nerve stimulation: Review of the state of the art," *J. Neuroeng. Rehabil.*, vol. 16, no. 1, pp. 1–16, 2019.

[9] B. Y. N. Accornero, G. Bini, G. L. Lenzi, and M. Manfredi, "Selective activation of peripheral nerve fibre groups of different diameter by triangular shaped stimulus pulses," *J. Physiol.*, vol. 273, no. 3, pp. 539–560, 1977.

[10] K. Y. Qing, M. P. Ward, and P. P. Irazoqui, "Burst-modulated waveforms optimize electrical stimuli for charge efficiency and fiber selectivity," *IEEE Trans. Neural Syst. Rehabil. Eng.*, vol. 23, no. 6, pp. 936–945, 2015.

[11] A. C. Thompson *et al.*, "Hybrid optogenetic and electrical stimulation for greater spatial resolution and temporal fidelity of cochlear activation," *J. Neural Eng.*, vol. 17, no. 5, 056046, 2020.

[12] A. A. Kühn *et al.*, "High-frequency stimulation of the subthalamic nucleus suppresses oscillatory β activity in patients with Parkinson's disease in parallel with improvement in motor performance," *J. Neurosci.*, vol. 28, no. 24, pp. 6165–6173, 2008.

[13] N. F. Ince *et al*., "Selection of optimal programming contacts based on local field potential recordings from subthalamic nucleus in patients with Parkinson's disease," *Neurosurgery*, vol. 67, no. 2, pp. 390–397, 2010.

[14] O. Yizhar *et al.*, "Neocortical excitation/inhibition balance in information processing and social dysfunction," *Nature*, vol. 477, no. 7363, pp. 171–178, 2011.

[15] G. Bilodeau *et al.*, "A wireless electro-optic platform for multimodal electrophysiology and optogenetics in freely moving rodents," *Front. Neurosci.*, vol. 15, pp. 1–15, 718478, 2021.

[16] L. L. Gagnon, G. Gagnon-Turcotte, A. Popek, A. Chatelier, M. Chahine, and B. Gosselin, "A wireless system for combined heart optogenetics and electrocardiography recording," *Proc. IEEE Int. Symp. Circuits Syst.*, Baltimore, MD, 2017.

[17] G. Gagnon-Turcotte, L. L. Gagnon, G. Bilodeau, and B. Gosselin, "Wireless brain computer interfaces enabling synchronized optogenetics and electrophysiology," *Proc. IEEE Int. Symp. Circuits Syst.*, Baltimore, MD, 2017.

[18] Y. Zhao *et al.,* "Wirelessly operated, implantable optoelectronic probes for optogenetics in freely moving animals," *IEEE Trans. Electron Devices*, vol. 66, no. 1, pp. 785–792, 2018.

[19] M. A. Rossi, V. Go, T. Murphy, Q. Fu, J. Morizio, and H. H. Yin, "A wirelessly controlled implantable LED system for deep brain optogenetic stimulation," *Front. Integr. Neurosci.*, vol. 9, pp. 1–7, 25713516, 2015.

[20] S. Il Park *et al.*, "Soft, stretchable, fully implantable miniaturized optoelectronic systems for wireless optogenetics," *Nat. Biotechnol.*, vol. 33, no. 12, pp. 1280–1286, 2015.

[21] P. Gutruf *et al.*, "Fully implantable optoelectronic systems for battery-free, multimodal operation in neuroscience research," *Nat. Electron.*, vol. 1, no. 12, pp. 652–660, 2018.

[22] Y. Jia *et al*., "A trimodal wireless implantable neural interface system-on-chip," *IEEE Trans. Biomed. Circuits Syst.*, vol. 14, no. 6, pp. 1207–1217, 2020.

[23] D. Jiang *et al.*, "An integrated bidirectional multi-channel opto-electro arbitrary waveform stimulator for treating motor neurone disease," *Proc. IEEE Int. Symp. Circuits Syst.*, Daegu, Korea, 2021.

[24] F. Liu, D. Jiang, and A. Demosthenous, "Towards a fully implantable closed-loop opto-electro stimulation interface for motor neuron disease treatment," *Proc. IEEE Int. Symp. Circuits Syst.*, Austin, Texas, 2022.

[25] N. Almarri, D. Jiang, and A. Demosthenous, "Design of a power management circuit for an opto-electro stimulator," *Proc. 19th IEEE Int. New Circuits Syst. Conf. (NEWCAS)*, Toulon, France, 2021.

[26] J. Avendaṇo-Coy, D. Serrano-Muṇoz, J. Taylor, C. Goicoechea-García, and J. Gómez-Soriano, "Peripheral nerve conduction block by high-frequency alternating currents: A systematic review," *IEEE Trans. Neural Syst. Rehabil. Eng.*, vol. 26, no. 6, pp. 1131–1140, 2018.

[27] W. M. Grill, *Model-Based Analysis and Design of Waveforms for Efficient Neural Stimulation*, 1st Ed., vol. 222. Elsevier B.V., 2015.

[28] C. K. Giardina, E. S. Krause, K. Koka, and D. C. Fitzpatrick, "Impedance measures during in vitro cochlear implantation predict array positioning," *IEEE Trans. Biomed. Eng.*, vol. 65, no. 2, pp. 327–335, 2018.

[29] V. G. Oklobdzija, "An algorithmic and novel design of a leading zero detector circuit: comparison with logic synthesis," IEEE Trans. Very Large Scale Integration (VLSI) Syst., vol. 2, no. 1, pp. 124-128, 1994

[30] D. Jiang, Y. Wu, and A. Demosthenous, "Hand gesture recognition using three-dimensional electrical impedance tomography," *IEEE Trans. Circuits Syst. II Express Briefs*, vol. 67, no. 9, pp. 1554–1558, 2020.

[31] Y. Liu, S. Luan, I. Williams, A. Rapeaux, and T. G. Constandinou, "A 64-channel versatile neural recording SoC with activity-dependent data throughput," *IEEE Trans. Biomed. Circuits Syst.*, vol. 11, no. 6, pp. 1344–1355, 2017.

[32] K. Abdelhalim and R. Genov, "Compact chopper-stabilized neural amplifier with low-distortion high-pass filter in 0.13μm CMOS," *Proc. 2012 IEEE Int. Symp. Circuits Syst.*, Seoul, Korea, pp. 1075–1078, 2012.

[33] A. Vanhoestenberghe and N. Donaldson, "Corrosion of silicon integrated circuits and lifetime predictions in implantable electronic devices," *J. Neural Eng.*, vol. 10, no. 3, 2013.

[34] G.Ziegelberger, *et al*., "Guidelines for limiting exposure to electromagnetic fields (100 kHz to 300 GHz), " Health Phys. ,vol. 118, no. 5, pp. 483–524, 2020.

[35] P. Kiele, P. Cvancara, M. Langenmair, M. Mueller, and T. Stieglitz, "Thin film metallization stacks serve as reliable conductors on ceramic-based substrates for active implants," *IEEE Trans. Components, Packag. Manuf. Technol.*, vol. 10, no. 11, pp. 1803–1813, 2020.

[36] D. Jiang *et al.,* "*A versatile hermetically sealed microelectronic implant for peripheral nerve stimulation applications,*" *Front. Neurosci.,* vol. 15, 681021, 2021.

[37] Thermal conductivity of tissues [Online]. Available: https://itis.swiss/virtual-population/tissue-properties/database/thermal-conductivity/

[38] A. Shon, J. U. Chu, J. Jung, H. Kim, and I. Youn, "An implantablewireless neural interface system for simultaneous recording and stimulation of peripheral nerve with a single cuff electrode," *Sensors (Basel)*, vol. 18, no. 1, pp. 1–26, 2018.

[39] J. Charthad *et al.*, "A mm-sized wireless implantable device for electrical stimulation of peripheral nerves," *IEEE Trans. Biomed. Circuits Syst.*, vol. 12, no. 2, pp. 257–270, 2018.

[40] H. Zhang *et al.*, "Wireless, battery-free optoelectronic systems as subdermal implants for local tissue oximetry," *Sci. Adv.*, vol. 5, no. 3, 2019.

[41] S. Y. Lee *et al.*, "A programmable wireless EEG monitoring SoC with open/closed-loop optogenetic and electrical stimulation for epilepsy control," *Dig. Tech. Pap. 2019 IEEE Int. Solid-State Circuits Conf. (ISSCC)*, pp. 372–374, 2019.

[42] BS EN 45502-1:2015, "Implants for surgery. Active implantable medical devices General requirements for safety, marking and for information to be provided by the manufacturer," ISBN: 978 0 580 72639 2.

[43] R. Erfani, F. Marefat and P. Mohseni, "A dual-output single-stage regulating rectifier with PWM and dual-mode PFM control for wireless powering of biomedical implants," *IEEE Trans. Biomed. Circuits Syst.*, vol. 14, no. 6, pp. 1195-1206, 2020.

[44] S. L. C. Au *et al.* "Injection molded liquid crystal polymer package for chronic active implantable devices with application to an optogenetic stimulator," *IEEE Trans. Biomed. Eng.*, vol. 67, no. 5, pp. 1357–1365, 2020.

Fangqi Liu

Fangqi Liu (Member, IEEE) received the B.Sc. degree from the Beijing University of Chemical Technology, Beijing, China, in 2012, the M.Sc. degree from the University of Leicester, Leicester, U.K., in 2014, and the Ph.D. degree in electronic and electrical engineering from University College London (UCL), London, U.K., in 2019. His PhD research focused on audio signal processing. He is currently a Postdoctoral Research Fellow with the Bioelectronics Group, Department of Electronic and Electrical Engineering, UCL. His current research interests include implantable and wearable devices, medical instrumentation, audio signal processing and biomedical interface system design.

Yu Wu

Yu Wu (Member, IEEE) received the B.Eng. degree in electronic and electrical engineering from University College London (UCL), London, U.K., in 2012, the M.Sc. degree in analog and digital integrated circuit design from Imperial College London, London, in 2013, and the Ph.D. degree in electronic and electrical engineering from UCL, in 2019. From 2016 to 2022, he was a Research Associate/Fellow with the Bioelectronics Group, UCL. He is currently a Lecturer with the Department of Electronic and Electrical Engineering, UCL. His current research interests include human-machine interactive systems, CMOS integrated circuit design, and novel mixed-signal microelectronic systems for biomedical applications.

Noora Almarri

Noora Almarri (Student Member, IEEE) received the B.S. degree in electrical engineering from New York University Abu Dhabi (NYUAD), United Arab Emirates, in 2019. She is currently working towards the Ph.D. degree in electronic and electrical engineering at University College London (UCL), U.K. She was part of the payload development team at NYUAD for the Rapid Acquisition Atmospheric Detector (RAAD), a detector designed to study terrestrial gamma ray flashes from space. Her current research interests include CMOS integrated circuit design, and optogenetics power management systems for biomedical applications.

Maryam Habibollahi

Maryam Habibollahi (Student Member, IEEE) received the M.Eng. degree from University College London (UCL), U.K., in 2019, where she is currently pursuing her Ph.D. degree, both in electronic and electrical engineering. Her research interests include the design and development of CMOS analog and mixed-signal integrated circuits for biomedical applications. Ms. Habibollahi was awarded an EPSRC Studentship to pursue her Ph.D. degree.

Henry T. Lancashire

Henry T. Lancashire received the B.Sc.(Hons.) degree in biomedical materials science from the University of Nottingham, Nottingham, U.K., in 2010, the M.Res. degree in molecular modeling and materials science from University College London (UCL), London, U.K., in 2011, and the Eng.D. degree in molecular modeling and materials science from UCL, London, U.K., in 2015. He was a Research Fellow with the Research Department of Materials and Tissue, UCL, from 2015 to 2017. In 2017, he joined the ASPIRE Centre for Rehabilitation Engineering and Assistive Technology, UCL as a Research Associate. Since 2018, he has been a Lecturer in active implantable medical devices with the Department of Medical Physics and Biomedical Engineering, UCL. His research interests include the micromanufacture, electrode properties, and biocompatibility, of active interfaces with nerve and muscle. Dr. Lancashire is a member of the Institute of Physics and Engineering in Medicine (IPEM) and a member of the Institute of Materials, Minerals and Mining (IOM3).

Barney Bryson

Barney Bryson is a Senior Fellow with the UCL Queen Square Institute of Neurology. His research is focused on the development of a novel strategy to restore lost muscle function, which has major therapeutic potential for ALS and other disorders that cause paralysis. His research utilizes stem cell derived components of the neuromuscular system to investigate pathological mechanisms that affect neuromuscular connections in ALS in a variety of in vitro and in vivo model systems, with the aim of identifying novel therapies that can protect these specialized connections and slow the course of progressive paralysis that occurs in ALS patients.

Linda Greensmith

Linda Greensmith is Professor of Neuroscience and Head of the Department of Neuromuscular Diseases at UCL. Her research focuses on understanding the molecular mechanisms that underlie ALS and SBMA, and the development of novel therapeutic strategies, using a range of tools including mouse models and iPSC-neurons.

Dai Jiang

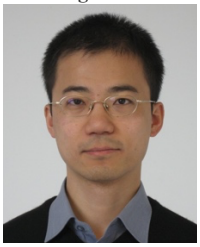

Dai Jiang (Senior Member, IEEE) received the B.Sc. and M.Sc. degrees from the Beijing University of Aeronautics and Astronautics, Beijing, China, in 1998 and 2001, respectively, and the Ph.D. degree from University College London (UCL), London, U.K., in 2009. His Ph.D. work was on frequency synthesis. He was with Datang Telecom Group, China, from 2001 to 2002, working on developing FPGA functions for WCDMA signal processing. From 2006 to 2020, he

was a Research Fellow with the Bioelectronics Group, UCL, where he is currently a Lecturer with the Department of Electronic and Electrical Engineering. His research interests include CMOS analog and mixed-signal integrated circuit design for biomedical applications. He is a Member of the Biomedical and Life Science Circuits and Systems Technical Committee of the IEEE Circuits and Systems Society.

Andreas Demosthenous

Andreas Demosthenous (Fellow, IEEE) received the B.Eng. degree in electrical and electronic engineering from the University of Leicester, Leicester, U.K., in 1992, the M.Sc. degree in telecommunications technology from Aston University, Birmingham, U.K., in 1994, and the Ph.D. degree in electronic and electrical engineering from University College London (UCL), London, U.K., in 1998. He is currently a Professor with the Department of Electronic and Electrical Engineering, UCL, and leads the Bioelectronics Group. He has made outstanding contributions to improving safety and performance in integrated circuit design for active medical devices, such as spinal cord and brain stimulators. He has numerous collaborations for cross-disciplinary research, both within the U.K. and internationally. He has authored more than 350 articles in journals and international conference proceedings, several book chapters, and holds several patents. His research interests include analog and mixed-signal integrated circuits for biomedical, sensor, communications, and signal processing applications. He is a Fellow of the Institution of Engineering and Technology and a Chartered Engineer. He was the co-recipient of a number of best paper awards and has graduated many Ph.D. students. He was an Associate Editor from 2006 to 2007 and the Deputy Editor-in-Chief from 2014 to 2015 of IEEE Transactions on Circuits and Systems II: Express Briefs, and an Associate Editor from 2008 to 2009 and the Editor-in-Chief from 2016 to 2019 of IEEE Transactions on Circuits and Systems I: Regular Papers. He is an Associate Editor for IEEE Transactions on Biomedical Circuits and Systems and serves on the International Advisory Board of Physiological Measurement. He served on the technical committees of international conferences, including the European Solid-State Circuits Conference and International Symposium on Circuits and Systems.